



Metabolic fate and subchronic biological effects of core-shell structured $\text{Fe}_3\text{O}_4@\text{SiO}_2\text{-NH}_2$ nanoparticles

Yueli Chen, Jinquan Li, Zhongxue Yuan, Jianghua Feng & Zhong Chen

To cite this article: Yueli Chen, Jinquan Li, Zhongxue Yuan, Jianghua Feng & Zhong Chen (2018) Metabolic fate and subchronic biological effects of core-shell structured $\text{Fe}_3\text{O}_4@\text{SiO}_2\text{-NH}_2$ nanoparticles, Nanotoxicology, 12:6, 621-636, DOI: [10.1080/17435390.2018.1471537](https://doi.org/10.1080/17435390.2018.1471537)

To link to this article: <https://doi.org/10.1080/17435390.2018.1471537>



View supplementary material [↗](#)



Published online: 10 May 2018.



Submit your article to this journal [↗](#)



Article views: 81



View Crossmark data [↗](#)

ARTICLE



Metabolic fate and subchronic biological effects of core-shell structured $\text{Fe}_3\text{O}_4@\text{SiO}_2\text{-NH}_2$ nanoparticles

Yueli Chen^{a*}, Jinquan Li^{a,b*}, Zhongxue Yuan^a, Jianghua Feng^a and Zhong Chen^a

^aDepartment of Electronic Science, Fujian Provincial Key Laboratory of Plasma and Magnetic Resonance, Xiamen University, Xiamen, China; ^bSchool of Pharmaceutical Science (Shenzhen), Sun Yat-sen University, Guangzhou, China

ABSTRACT

Core-shell structured $\text{Fe}_3\text{O}_4@\text{SiO}_2\text{-NH}_2$ nanoparticles ($\text{Fe}@\text{Si-NPs}$) demonstrated outstanding potentials in drug targeting and delivery and medical imaging. However, they have limited clinical applications due to unknown chronic bio-effects and potential bio-related risks. In this study, the subchronic biological effects and metabolic fate of 20 nm $\text{Fe}@\text{Si-NPs}$ in Sprague–Dawley rats in 12 weeks were investigated by the biochemical assay and NMR-based metabonomic analysis using an intravenous model. Biofluids (plasma and urine) analysis provided the transportation, absorption, and excretion information of $\text{Fe}@\text{Si-NPs}$. Urine metabonome displayed a metabolic recovery while self-regulation of plasma metabonome led to the parallel metabolic trends between dosed and control groups in 12 weeks. And biological tissues (spleen, liver, kidney, and lung) analysis indicated liver and spleen are the targeted-organs of $\text{Fe}@\text{Si-NPs}$. The obvious metabolic variations responding to the biodistribution were induced by $\text{Fe}@\text{Si-NPs}$ although no visible toxic effects were observed in these tissues. Besides the common energy metabolism response to the xenobiotics, $\text{Fe}@\text{Si-NPs}$ also disturbed the metabolic pathways in glycerophospholipid and sphingolipid metabolism, metabolisms of purine, pyrimidine, and nicotinate. Our results provide preliminary validation for the potential use of $\text{Fe}@\text{Si-NPs}$ in clinical medicine and give identifiable ground for the dose selection and bio-nanoagent optimization.

ARTICLE HISTORY

Received 16 January 2018
Revised 17 April 2018
Accepted 27 April 2018

KEYWORDS

Core-shell structure;
biomedical nanoparticles;
subchronic biological effect;
metabonomics

1. Introduction


Magnetic core-shell structured nano-materials (Javidi et al. 2015), which combine features of magnetic cores and various functional shells, have gained much attention and undergone intensive investigation due to their unique magnetic properties, good stability (Abramson et al. 2011), biological safety (Shao et al. 2011), and low cytotoxicity (Liu et al. 2012; Wu et al. 2012). Especially, their chemically modifiable surfaces expand the potential applications in medicinal environment, optical, and chemical imaging as the supporting material (Kong et al. 2012; Hu et al. 2014). However, they have been proved to bring damage to living animal. An earlier study reported that $\text{Fe}_3\text{O}_4@\text{SiO}_2$ caused the liver damage and induced metabolic perturbation in rats (Kim et al. 2008). Therefore, many functionalized $\text{Fe}_3\text{O}_4@\text{SiO}_2$ nanoparticles with high stability and

high solubility have been successfully synthesized to improve the biocompatibility.

Recently, amino-functionalized $\text{Fe}_3\text{O}_4@\text{SiO}_2$ nanoparticles ($\text{Fe}@\text{Si-NPs}$), a new type of multilayer and multifunctional magnetic nanospheres, have provided clinical advantages over the existing $\text{Fe}_3\text{O}_4@\text{SiO}_2$ nanoparticles. In the multilayer structure, the magnetic core (iron oxide nanoparticles) provides many unique advantages including high surface area, ease for synthesis and modification, and high magnetic superparamagnetic properties (Zhan et al. 2014). And the inner layer silica can protect the magnetically responsive core from corrosion oxidation and dispersion during the blood circulation. Moreover, the outer layer of amino group has good hydrophilicity, which can prolong the blood circulation time of the particles and enhance its stability. Studies have shown that

CONTACT Jianghua Feng ✉ jianghua.feng@xmu.edu.cn Department of Electronic Science, Fujian Provincial Key Laboratory of Plasma and Magnetic Resonance, Xiamen University, Xiamen, China

*These authors have contributed equally to this work.

 Supplemental data for this article can be accessed [here](#).

© 2018 Informa UK Limited, trading as Taylor & Francis Group

amino-modified nanocomposites demonstrated better adsorption properties and higher specific enzymatic activity for plasmid DNA (Xu et al. 2012) and bovine hemoglobin (Wang et al. 2015) than unmodified materials (Slovakova et al. 2015). Due to its ultra-fine particle size, good stability, and biocompatibility, Fe@Si-NPs show great potential in biomedical fields such as magnetic resonance imaging, disease diagnosis, and drug transport (Xu et al. 2012).

Previous research (Khlebtsov and Dykman 2011) indicated that several factors, including particle type and size, surface modification, doses, and method of administration, will affect the potential adverse effects and biological fate of nanoparticles. In some early articles, it was noted that injection of metallic gold may lead to inflammatory responses (Oberdorster et al. 2005; Chen et al. 2009; Moyano et al. 2012) and oxidative stress (Oberdorster et al. 2005; Chen et al. 2006; Ahamed et al. 2011; Shi et al. 2013) of animals, and gold would accumulate in the reticular cells of lymphoid tissue (Chen et al. 2009; Ahamed et al. 2011; Hirn et al. 2011) and take a long-term effects on the activation of cellular and humoral immunity. Xie et al. (2010) proved that Si-based nanoparticles are retained for over 30 days in the tissues and accumulate mainly in lungs, liver, and spleen, and thus could potentially cause liver injury. Meike et al (van der Zande et al. 2012) observed that silver nanoparticles present in all examined organs with the highest levels in the liver and spleen for all treatments and were cleared from most organs after 8 weeks post-dosing. In contrast, other researches proved nanoparticles induced *in vivo* low toxicity to mice over 3 months (Yang et al. 2008; Xiong et al. 2010).

When such nanoparticles are functionalized with chemical groups designed to permit the specific attachment of drugs, it is necessary to understand their potential toxicological effects and metabolic responses before moving to clinical tests. Although the tissues in which most Fe@Si-NPs are *in vivo* located are clear (Sonavane et al. 2008), time-dependent and quantitative information about the distribution of Fe@Si-NPs in these tissues is lacking. It is important to understand how long and what quantity of nanoparticles are retained, as well as why nanoparticles accumulate in these tissues for their clinical translation. Therefore, monitoring the

quantitative biodistribution of Fe@Si-NPs and analyzing the localization mechanism will improve our understanding of their efficacy and side effects for the pharmacological use. In drug safety studies, NMR-based metabonomics can identify target organs, acquire toxic biochemical mechanisms, and identify biochemical markers for disease onset and progression. It has been proved to be an effective method to evaluate the nanotoxicity in previous study (Feng et al. 2002; Li et al. 2013, 2014). Thus, investigation of *in vivo* metabolic changes induced by nanoparticles may provide a detailed description of the corresponding bio-response.

In this study, we evaluate the subchronic biological response in rats to an intravenous injection of Fe@Si-NPs and investigate their biodistribution and metabolic fate by combining ^1H NMR-based metabonomic strategy with the traditional biochemical methods including blood biochemical analysis and ICP-AES determination of Fe concentration in tissues. Moreover, the factors influencing the potential adverse effects of Fe@Si-NPs were analyzed, and the existing problems and challenges in toxicological researches of iron-based nanoparticles were summarized.

2. Materials and methods

2.1. Synthesis and characterization of core-shell structured nanoparticles

The amino-functionalized core-shell structured nanoparticles (Fe@Si-NPs) were synthesized by a multistep process as reported previously (Wang et al. 2011). In brief, monodisperse superparamagnetic Fe_3O_4 nanoparticles were first prepared using the modified solvothermal method (Zhang et al. 2010), and the prepared Fe_3O_4 nanoparticles were then coated with a layer of nonporous silica to form $\text{Fe}_3\text{O}_4@\text{SiO}_2$ spheres via the hydrolysis of a solgel precursor (Vivero-Escoto and Huang 2011). Finally, an amino functionalized layer was condensed over the particles via hydrolysis and condensation of N-(2-aminoethyl)-3-aminopropyl trimethoxysilane (AEAPS). The diameters of iron oxide core vary from 2.3 to 4.0 nm and the corresponding Fe@Si-NPs are approximately 20 nm. The obtained Fe@Si-NPs were vacuum dried at 80 °C and characterize by FTIR and TEM (Figure S1 in the supplemental materials). And the zeta potentials of Fe_3O_4 , $\text{Fe}_3\text{O}_4@\text{SiO}_2$, and

Fe@Si-NPs at pH 7.0 were measured on a Nano-ZS (Malvern Instruments Ltd., UK) to be -20 , -40 and -28 mV, respectively. The Fe@Si-NPs were freshly dispersed by ultrasound in saline solution before use. In detail, the nanoparticles suspension was subjected to high speed centrifugation at $12\,000g$ for 10 min. After the removal of the supernatant, the Fe@Si-NPs were resuspended in phosphate buffer saline (PBS, pH 7.4) and sonicated for 60 s ($6s \times 10$ times) at 200 W to uniformly disperse. The ultrasonic temperature was set as $31-39^\circ\text{C}$. Hydrodynamic sizes of the Fe@Si-NPs were measured by dynamic light scattering (DLS), and the effective hydrodynamic diameter was about 42 nm, confirming that Fe@Si-NPs were well-dispersed in saline.

2.2. Animal handling and sample collection

The experimental protocols complied with the local Guidelines for Animal Use and Care and were approved by the Ethical and Research Committee of Xiamen University. All of the animal experiments were performed at specific pathogen free (SPF) facility of Xiamen University Laboratory Animal Center. A total of 25 eight-week-old Sprague-Dawley rats (284.5 ± 15.6 g) were used in our study. After a 12-day acclimatization (under standard experimental condition: $21-26^\circ\text{C}$, 45–70% relative humidity, 12:12-h light-dark cycle, and free access to food and tap water), a single dose of Fe@Si-NPs was administered intravenously to the rats. The injected doses were 1 mg Fe/kg body weight (b. w.) in low-dose group ($n=8$) and 5 mg Fe/kg b. w. in high-dose group ($n=9$), respectively, while the maximum injection volume is no more than 1 mL each rat. The selection of doses was determined by the imaging efficiency of Fe@Si-NPs as MRI contrast agent and the clinical dose of ultrasmall superparamagnetic iron oxide (USPIO) (Saini et al. 2000). And the control group ($n=8$) was treated with saline only. Individual urine samples were collected in ice-cooled vessels containing 0.1 g/mL sodium azide (20 μL) for 2 h using a metabolic cage at time point of 0, 1, 2, 4, 8, and 12 week post-dose (p. d.) and immediately frozen at -80°C . Orbital blood sample (1 mL) was collected by exsanguination under isoflurane anesthesia at time point of 2, 4, 8, and 12 w p. d. and divided into two aliquots, one serum for biochemical analysis and the other heparinized

plasma for NMR spectroscopic analysis. All rats were sacrificed by cervical dislocation for tissue sample collection at 12th w p. d. After weighting, the kidney, liver, lung, and spleen were excised into duplicate and snap-frozen in liquid nitrogen for tissue extraction and ICP-AES analysis, and then immediately stored at -80°C until use.

2.3. Biochemical assay of serum

Standard spectrophotometric methods were used to measure the following biochemical parameters on a Roche Modular P800 automatic analyzer (Roche Diagnostics, Germany): total protein (TP), albumin (Alb), globulin (Glo), Alb/Glo, total bilirubin (Tbil), direct bilirubin (Dbil), indirect bilirubin (Ibil), alanine aminotransferase (ALT), aspartate aminotransferase (AST), AST/ALT, gamma glutamyltransferase (GGT), alkaline phosphatase (ALP), triglycerides (TG), total cholesterol (TC), high density lipoprotein (HDL), low-density lipoprotein (LDL), glucose (Glu), lactate dehydrogenase (LDH), blood urea nitrogen (Bun), creatinine (Cn), Bun/Cn, uric acid (UA), and total bile acid (TBA). All parameters are expressed as mean \pm standard deviation (SD).

2.4. Histopathology

Selected samples of liver, spleen, kidney, and lung tissues from Fe@Si-NPs-treated and control rats were fixed in 10% formalin. After that, wax-embedded sections (5 μm) were cut, and stained with hematoxylin and eosin for histopathological examination under a microscope.

2.5. Sample preparation and NMR experiments

The sample preparation was carried out according to the established protocol (Feng et al. 2002). In brief, plasma sample (200 μL) was mixed with 400 μL of deuterated phosphate buffer (90 mM, pH 7.4) to minimize any gross variation in the pH of the samples. After centrifugation at $10\,000g$ at 4°C for 10 min to remove the precipitates, 500 μL of the supernatants was transferred into a 5-mm NMR tube for NMR spectroscopy.

Urine sample (500 μL) was mixed with 50 μL of deuterated phosphate buffer solution ($\text{K}_2\text{HPO}_4/\text{NaH}_2\text{PO}_4$, 1.5 M, pH 7.4, D_2O). After centrifugating at

10 000 *g* at 4 °C for 10 min to remove the precipitates, 500 μ L of the supernatants were transferred into a 5-mm NMR tube for NMR spectroscopy. ^1H NMR spectra of plasma and urine samples were acquired on a 500 MHz Varian spectrometer operating at 499.74 MHz at 296 K. ^1H NMR spectra for plasma samples were acquired with a standard water-suppressed CPMG pulse sequence. For each plasma sample, 64 free induction decays (FIDs) were collected into 20 K data points over a spectral width of 10 kHz with a relaxation delay of 1 s and an acquisition time of 2 s. Spin-echo loop time ($2n\tau$) was set as 70 ms. For each urine sample, a standard NOESYPR1D pulse sequence was used, and 64 FIDs were collected into 26 K data points over a spectral width of 10 kHz with a relaxation delay of 1.4 s and an acquisition time of 2.60 s. The water resonance was selectively irradiated during the relaxation delay and the mixing time.

Pre-weighted tissue samples (kidney, liver, lung, and spleen samples, 100 mg per sample) were homogenized in 400 μ L of CH_3OH and 85 μ L of H_2O at 4 °C. The homogenates were transferred to a 2.5 ml EP tube, combined with 400 μ L of CHCl_3 and 200 μ L of H_2O , and vortexed for 60 s. After 10 min partition on ice, the samples were centrifuged for 5 min at 2000 *g* at 4 °C. The upper supernatants were transferred to 1.5 mL tubes, and lyophilized to remove CH_3OH and H_2O . The extracts were reconstituted to 500 μ L D_2O containing 0.05% TSP and transferred into 5 mm NMR tubes, and then analyzed by NMR spectroscopy. NMR measurements of tissue samples were carried out on a 600 MHz Bruker spectrometer at 298 K operating at 600.13 MHz with a standard NOESYPR1D pulse sequence. For each sample, 64 FIDs were collected into 32 K data points over a spectral width of 12 kHz with a relaxation delay of 2 s and an acquisition time of 2.65 s.

2.6. NMR spectral processing

For all ^1H NMR spectra, FIDs were multiplied by an exponential function with a 1 Hz line-broadening factor prior to Fourier transform to increase the signal-to-noise ratio. All the ^1H NMR spectra were manually phased and baseline-corrected using MestReNova (V9.0, Mestrelab Research, Santiago de Compostela, Galicia, Spain). In plasma samples, the

chemical shifts were referenced to the internal lactate CH_3 resonance at δ 1.33, and the spectral regions of δ 5.95–5.55 and δ 5.2–4.29 were removed to exclude the urea signal and uncertainty of residual water signal. The remainder spectral region δ 9.5–0.5 was divided into 0.002 ppm integral segments. When preprocessing urine and tissues spectra, the chemical shifts were referenced to TSP at δ 0.00, and then the spectra were segmented into 0.01 ppm integrals. In order to eliminate the interference of methanol and residual water signal, the spectral region of δ 5.2–4.6 in urine spectra and δ 5.12–4.57 and δ 3.37–3.35 in tissues spectra were removed. All the disposed data were normalized to the total sum of the spectrum, which made the data directly comparable with each other.

2.7. Univariate and multivariate statistical analyses

To get insight into the bio-information contained in NMR spectra, multivariate statistical analysis was carried out with software package SIMCA (V14.0, Umetrics AB, Umeå, Sweden). Principal component analysis (PCA) was conducted by using a mean-centered scaling approach. To maximize separation and better understand the specific metabonomic difference between Fe@Si-NPs-treated group and control group, orthogonal projection to latent structure with discriminant analysis (OPLS-DA) algorithm at a parato (Par) scaling approach was further performed. The results were visualized in the forms of scores plots to show the group clusters and loadings volcano plots to show the metabolites associated to clustering. For better reliability of characteristic metabolites' screening, the relative concentrations of metabolites were compared through calculating the integral area of corresponding signals, which represented as fold changes, and then the *p* value of statistical analyzed with Student's *t*-test were obtained. In the loading volcano plots, *X* axis indicated as $-\log_2$ of fold changes in concentration and *Y* axis indicated as $-\log_{10}$ of *t*-test statistically *p* value; The color indicated the coefficient of correlation, represent the significant difference between classes where a hot color corresponds to the significant difference between classes while a cool color corresponds to no significant differences; The size of dot indicated

Figure 1. Typical ^1H NMR spectra of urine, plasma and the aqueous extracts of lung, kidney, spleen and liver from a low-dose Fe@Si-NPs treated rat at 12th week post-dose. The regions of δ 6.3–9.5 (in the dashed box) in the spectra were magnified 8 times in vertical expansion compared with the corresponding regions of δ 0.5–6.2 for the purpose of clarity. Keys for the assignments are shown in [Table S1 in the supplemental materials](#).

functions. For example, the remarkable resonances of glucose, glycogen and various amino acids in hepatic spectra are strongly associated with the biological roles of supporting homeostasis, converting molecules and regulating energy balances of the liver. The obvious peaks of creatinine and creatine in renal spectra are related to the secretory function of kidneys. While the waste metabolites such as formate, acetate, butyrate, urea, hippurate, and phenylacetylglycine in urinary spectra are the results of excretion and activity of the intestinal flora.

3.2. Metabolic trajectory following Fe@Si-NPs administration and biological responses in biofluids

To get the overall metabolic information and identify general metabolic trends following Fe@Si-NPs administration, metabolic trajectories in plasma and urine of rats in 12 week p. d. were obtained with PCA from the respective NMR data sets. Basically, the average PCA scores plots showed obvious metabolic trajectories following Fe@Si-NPs treatments and demonstrated substantial metabolic variations in treated groups (Figure 2). Unexpectedly, obvious metabolic differences still could be observed between both low- and high-dosed groups and the controls at 4th week p. d. both in plasma and urine metabonomes. Thereafter, a metabolic recovery was observed in the urine metabonome especially at 12th week p. d. (Figure 2(B)) while no obvious metabolic recovery was displayed in plasma metabonome (Figure 2(A)). The plasma metabonomes in

dosed rats did not recover to the normal physiological states but they developed in a parallel way to the control group. Such differences in the metabolic profiling indicate that plasma metabonomes are more sensitive than urine metabonomes to Fe@Si-NPs treatment, but the self-regulation ability of plasma leads to the similar metabolic trends between dosed and control rats.

3.2.1. Metabonomic responses of plasma to Fe@Si-NPs treatments

It seems that the 4th week p. d. is a critical time point for the biological response of plasma metabonome. Obvious dose-effect was observed in 4 weeks p. d., where low-dose groups showed a close distance but high-dose groups separated from the controls (Figure 2(A)), which indicated more metabolic disturbance of plasma in rats induced by high concentration Fe@Si-NPs. The OPLS-DA scores plot give a significant ($p < 0.05$) separations between control and high-dose group (Figure 3), and the volcano plot (Figure 3) indicated that high-dose Fe@Si-NPs induced the elevated levels of alanine, betaine, ethanol, glutamate and leucine and the reduced level of 3-hydroxybutyrate (3-HB), isobutyrate and N-Acetyl-glycoproteins (NAS).

Leucine is an essential amino acid in the diet of animals, partially protects muscle mass and function. A high level of leucine may interfere with the conversion of tryptophan to niacin (Wang et al. 2018). Alanine is the most effective precursor for gluconeogenesis (Schindhelm et al. 2006).

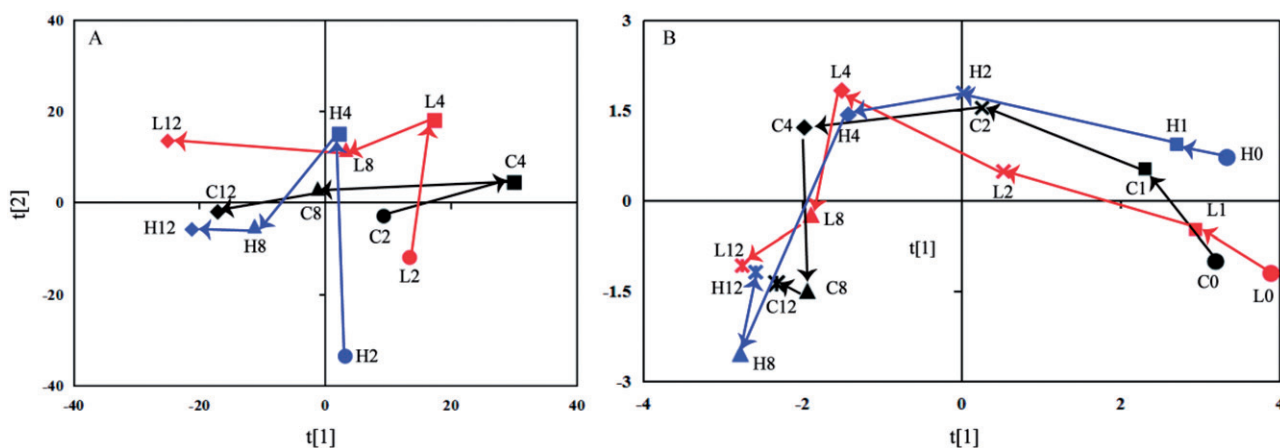


Figure 2. Metabolic trajectories of Si@Fe-NPs in plasma (A) and urine (B) of rats. C: control group; H: high-dose group; L: low-dose group; 0: pre-dose; 1–12: 1–12 week post-dose. Each point (shown as circle, box, cross, diamond, triangle or star) presents as the mean for each group.

Isobutyrate is prepared by the oxidation of isobutyraldehyde, which is a byproduct of the hydroformylation of propylene (Eckerle 2001). The alterations of above substances indicated that Fe@Si-NPs interfere with the biosynthesis of amino acid.

As an important nutrient for the prevention of chronic disease, betain is the source of methyl groups, while the methylation process helps the body to respond to stress by participating in the methionine cycle primarily in the human liver and kidneys (Craig 2004). Plasmatic 3-HB can be formed during fatty acid oxidation, and its depletion in Fe@Si-NPs exposed group suggests a response to the decreased energy demand resulting in the decreased gluconeogenesis in organisms. Besides, changed glutamine level suggests that the carbon metabolism for the production of energy was disturbed.

Glutamate is used by almost all living beings in the biosynthesis of proteins. Ammonium is synthesized predominantly in the liver and finally excreted from the body in the form of urea (Grabowska et al. 2011). Glutamate plays an important role in the body's disposal of excess nitrogen as an intermediate. The alterations of glutamate and allantoin (Table S2) reveal that Fe@Si-NPs disturbed the normal recycling of urea.

3.2.2. Metabonomic responses of urine to Fe@Si-NPs treatments

Analysis of the urinary metabonomes may provide the time- and dose-response information of Fe@Si-NPs that can be used to determine the onset and severity of adverse effects. The univariate and multivariate statistical results (Figure 3 & Table S3) indicated that Fe@Si-NPs result in an increase of

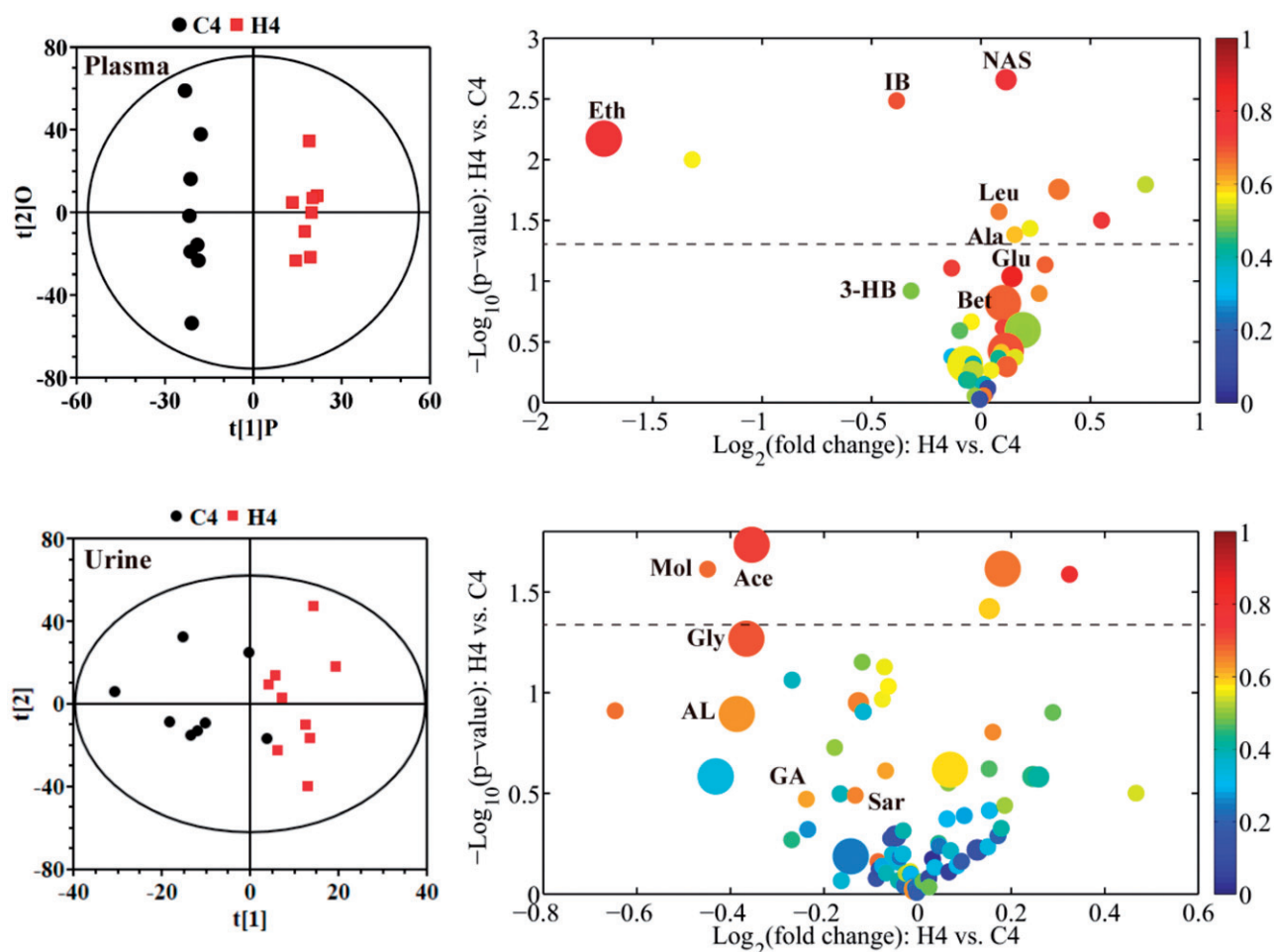


Figure 3. OPLS-DA scores plots (left panels) and corresponding volcano plots (right panels) derived from ^1H NMR spectra of plasma and urine samples obtained from the different pair-wise groups. C and H represent the control and high-dose groups, respectively; and 4 represent 4th week post-dose. The marked circles in the volcano plots represent the differential metabolites. Keys for the assignments are shown in Table S1 in the supplemental materials.

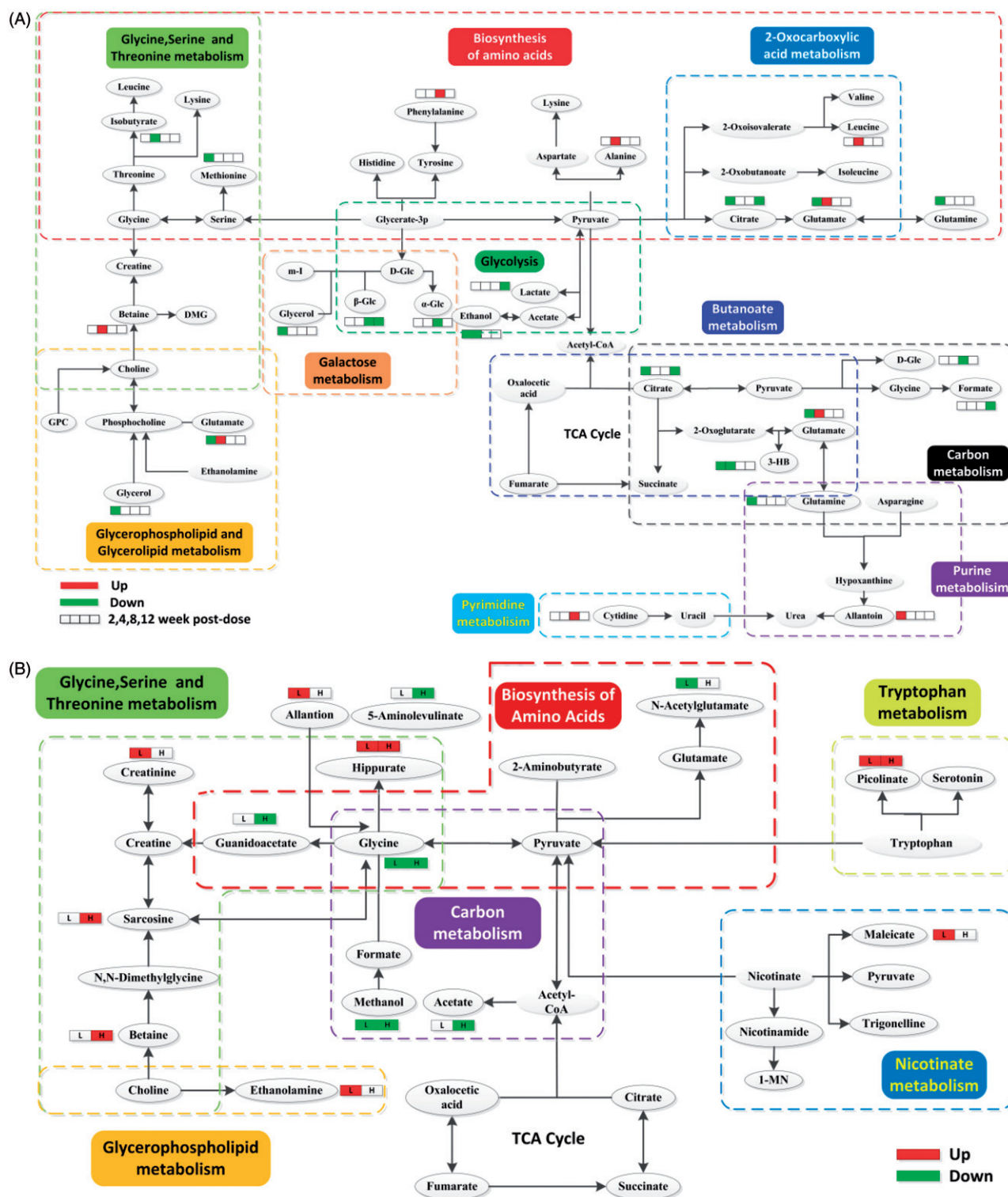


Figure 4. The metabolic networks involved in transportation, absorption, secretion, and excretion Fe@Si-NPs via the metabonomic variations in plasma of high-dose groups (A) and urine at 4th week post-dose (B). The decreased and increased levels and no significant change of the differential metabolites against the corresponding controls are represented by green, red and blank boxes. The different background colors for the pathways indicate the different biochemical pathways. Keys for the assignments are shown in Table S1 in the supplemental materials.

allantoin, betaine, creatinine (Cn), ethanolamine, hippurate, maleicate, picolinate and sarcosine together with a decrease of 5-aminolevulinate, acetate, glycine, guanidoacetate (GA), methanol and N-acetylglutamate (NAG) in 4 weeks p. d.

Sarcosine is an intermediate in the metabolism of choline to glycine. Previous study reported that sarcosine may activate cancer cells and indicate the malignancy when measured in urine (Sreekumar et al. 2009). GA is an enzyme that is synthesized from arginine and glycine, and consumes a methyl group to form creatine. Cn is filtered from the blood by the kidneys and released into the urine, so urinary Cn levels are usually a good indicator of how well the kidneys work. In our case, the increase of urinary creatine and Cn excretion may suggest kidney disease or functional disturbance. Hippurate is synthesized from benzoate and glycine. A rise in hippurate level and a decline in glycine level in urine treatment groups at 4 w p. d. (Table S3) suggest that Fe@Si-NPs could interfere with benzoate metabolism and excretion.

Acetate is a common anion in biology. It is mainly utilized by organisms in the form of acetyl coenzyme A (Koplove 1984). Maleicate is a dicarboxylic acid. And 5-aminolevulinate is an endogenous non-protein amino acid. Uric acid is the end product of the purine metabolism. Fe@Si-NPs

induced the variations in these organic acids in the urine, implying the disturbed excretion process. Only non-enzymatic processes with reactive oxygen species will give rise to allantoin, which is thus a suitable biomarker to measure oxidative stress in chronic illnesses and senescence (Zitnanova et al. 2004; Kand'ar and Zakova 2008).

3.2.3. Transportation, absorption, secretion and excretion of Fe@Si-NPs

A global analysis based on the potential biomarkers can provide an overall impression of the biological effects induced by Fe@Si-NPs. To identify the most relevant metabolic pathways involved in metabolic disturbance of Fe@Si-NPs-treated rats, the differential metabolites were further subjected to MetaboAnalyst. Accordingly, the integrated metabolic networks (Figure 4) could be derived from the metabonomic variations of plasma and urine.

Plasma provides the medium for the functionalization of Fe@Si-NPs, and its metabonomes variations are closely related to the transportation and absorption of Fe@Si-NPs. According to the metabolic networks in plasma (Figure 4(A)), the disturbed metabolic pathways include glycerophospholipid and glycerolipid metabolism, purine and pyrimidine metabolisms, and carbon metabolism besides the common metabolic responses such as energy

Table 1. Effect of Fe@Si-NPs administration on blood biochemical indexes for rats at 12th week post-dose.

Indexes	C ^a	L	H
Total protein (TP)	67.40 ± 3.08	68.45 ± 1.95	66.63 ± 3.41
Albumin (Alb)	32.41 ± 0.95	32.35 ± 0.57	31.79 ± 1.19
Globulin (Glo)	33.74 ± 5.64	36.10 ± 1.61	34.84 ± 2.59
Alb/Glo	0.93 ± 0.04	0.90 ± 0.03	0.92 ± 0.06
Total bilirubin (Tbil)	2.60 ± 0.20	2.60 ± 0.19	2.73 ± 0.28
Direct bilirubin (Dbil)	0.95 ± 0.11	1.01 ± 0.08	1.00 ± 0.11
Indirect bilirubin (Ibil)	1.65 ± 0.14	1.59 ± 0.11	1.73 ± 0.19
Alanine aminotransferase (ALT)	52.38 ± 8.14	49.38 ± 9.38	49.22 ± 8.74
Aspartate aminotransferase (AST)	179.88 ± 36.17	142.88 ± 25.64*	138.67 ± 32.42*
AST/ALT	3.47 ± 0.73	2.92 ± 0.35	2.82 ± 0.46*
Gamma glutamyltransferase (GGT)	0.21 ± 0.32	0.55 ± 0.48	0.40 ± 0.45
Alkaline phosphatase (ALP)	112.88 ± 14.30	119.38 ± 22.05	120.11 ± 32.59
Triglycerides (TG)	1.68 ± 0.46	1.39 ± 0.53	1.78 ± 0.83
Total cholesterol (TC)	2.26 ± 0.32	2.42 ± 0.40	2.19 ± 0.32
High density lipoprotein (HDL)	0.63 ± 0.08	0.70 ± 0.12	0.63 ± 0.13
Low-density lipoprotein (LDL)	0.16 ± 0.04	0.16 ± 0.03	0.13 ± 0.03
Glucose (Glu)	5.14 ± 0.93	5.18 ± 0.74	5.27 ± 0.81
Lactate dehydrogenase (LDH)	582.59 ± 263.73	769.01 ± 207.95	832.17 ± 320.19
Blood urea nitrogen (Bun)	5.93 ± 0.69	5.80 ± 0.82	6.49 ± 0.62
Creatinine (Cn)	57.88 ± 3.48	58.88 ± 5.89	56.67 ± 2.60
Bun/Cn	0.10 ± 0.01	0.10 ± 0.01	0.11 ± 0.01
Uric acid (UA)	116.25 ± 21.24	95.25 ± 11.26*	124.22 ± 26.68
Total bile acid (TBA)	19.89 ± 9.72	18.46 ± 9.09	14.92 ± 8.06

Each value represents the mean ± SD.

*Significant difference from the controls as judged by Student's *t*-test (**p* < 0.05).

^aC: control group; H: high-dose group; L: low-dose group.

metabolism (glycolysis and galactose metabolism), biosynthesis and metabolism of amino acid, carboxylic acid metabolism response to the xenobiotics in organisms.

As the end-point of excretory system, the metabonomic variations of urine will provide the detailed secretory and excretory bio-information of Fe@Si-NPs. From the metabolic networks related to secretion and excretion (Figure 4(B)), the significantly fluctuated metabolic pathways in urine include biosynthesis and metabolism of amino acids, glycerophospholipid metabolism, nicotinate metabolism, and carbon metabolism as identified by the corresponding discriminatory metabolites above.

3.3. Biodistribution and biological effects and fate of Fe@Si-NPs

3.3.1. Effect of Fe@Si-NPs on serum biochemical parameters

In clinical practice, the blood biochemical indexes are often used to determine tissue function especially for renal and hepatic functions. In our study, serum biochemistry assays were used to evaluate more quantitatively the influence of Fe@Si-NPs on the exposed rats. As shown in Table 1, the two important hepatic indicators, ALT and AST, as well as the ratio of AST/ALT, decreased in the dosed groups, especially in the high-dosed groups. Although the lower value of AST and ALT is clinically insignificant, the reduction of AST/ALT in serum is one of the characteristics of chronic hepatitis or

cirrhosis (Williams and Hoofnagle 1988; Gurung et al. 2013). In the high dose-group, AST/ALT showed a lower level than that in the control group. We think that the decrease of AST and AST/ALT may be due to the mild inflammation caused by nanoparticles, which could be supported by the increased inflammatory cells in the liver of the high-dose group (Figure S2). LDH is an enzyme widely present in cytosol that converts lactate to pyruvate, which can leak into blood through the damaged cell membrane during the pathological changes of organs and tissues, causing an increase of the serum LDH level. The concentrations of LDH increased to 132% ($p < 0.10$) in the low-dose group and 143% ($p < 0.10$) in the high-dose group, which may be due to this non organ-specific cell damage induced by Fe@Si-NPs. The concentrations of blood urea nitrogen and uric acid were also observed to increase in high-dosed group though not significantly. These changes indicated that renal function could be disturbed by Fe@Si-NPs exposure in high-dosage.

3.3.2. The ratios of tissue to body weights and iron biodistribution in tissues

The fluctuations in body weight and tissue/body ratio are useful indicators for studying the adverse effects of nanoparticles, especially for the chronic effect. Figure 5 (left panel) shows the tissue/body ratios after 12 weeks of intravenous injection, which suggest no significant difference between two dosed groups and control group as judged by

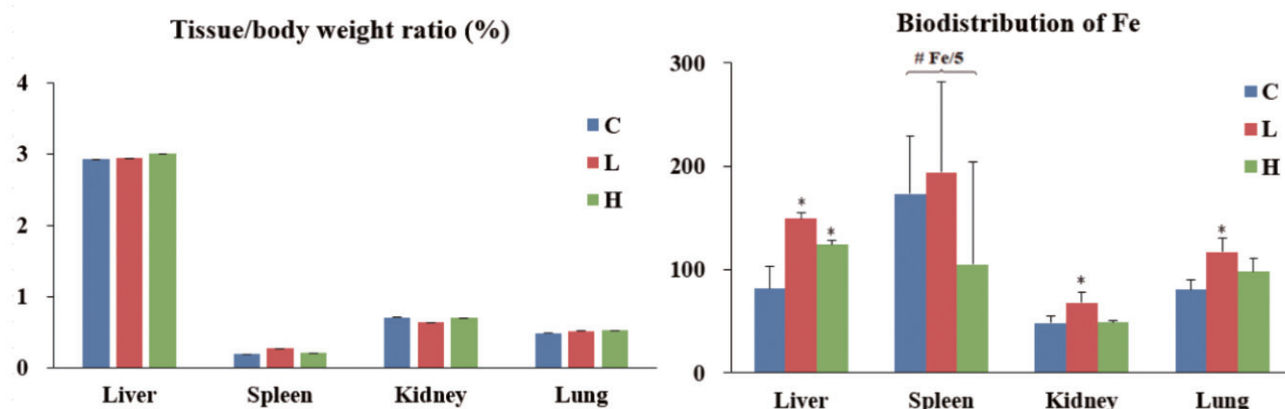


Figure 5. Effect of Fe@Si-NPs administration on tissue/body weight ratio (in %) (left panel) and biodistribution of Fe (right panel) in rat tissues at 12th week post-dose. C: control group; H: high-dose group; L: low-dose group. *Significant difference from the controls as judged by Student's *t*-test ($*p < 0.05$). #To better display the data of each group, the content of Fe in spleen in the figure is 1/5 of the actual content.

Student's *t*-test. Over a period of 12 weeks, the body weight of the Fe@Si-NPs-treated rats increased in a pattern similar to that of the control rats, suggesting that the rats had been continuing to grow up without visible toxic effects.

The distribution of Fe@Si-NPs in tissues in 12 weeks p. d. was evaluated by ICP-AES (right panel in Figure 5). The result shows that most of the nanoparticles were transferred into spleen and liver, suggesting that spleen and liver are the main specific-targeted organs of Fe@Si-NPs, especially, the Fe content in spleen is much higher than that in other tissues. Such biodistribution also confirmed that iron-based nano-agents are usually used for the reticuloendothelial system such as the liver and spleen. Furthermore, the contents of Fe in low-dose group significantly increased ($p < 0.05$) in liver, kidney, and lung, while that in high-dose group increased only in liver. Previous study (Yang et al. 2008) had proved that most of iron-based nanoparticles would be transferred to tissue after 1 week p. d. with the increase of Fe. In our study, the concentration of Fe in high group was lower than in low-dose group, and showed no significant increase in the 12th week, which may be due to their different biochemical mechanisms in transportation, biodistribution and secretion. The high-dose Fe@Si-NPs tend to rapidly clear from circulation but may bring bigger disorder to the living metabolism (Gupta and Gupta 2005). Especially, the concentration of Fe in spleen in high-dose group showed decrease to 57% of the controls but with a larger standard deviation, which may attribute to the visible hypersplenotrophy in a few rats due to inflammation induced by Fe@Si-NPs.

3.3.3. Effects of Fe@Si-NPs on gross histological changes

Histopathological examinations were conducted on selected animal tissues from control and Fe@Si-NPs groups (Figure S2). Portal area of liver and hepatocytes around the central vein show normal, however, the high-dosage Fe@Si-NPs induced the increased inflammatory cells in the liver parenchyma (Figure S2(C)). No apparent pathological change was observed in the other tissues including spleen (Figure S2(E & F)), kidney (Figure S2(H & I)), and lung (Figure S2(K & L)) of the Fe@Si-NPs groups

compared with the controls (Figure S2(D), (G), and (J)), respectively.

3.3.4. Metabonomic responses to Fe@Si-NPs treatments in the tissues

The OPLS-DA scores plots (left panels in Figure 6) give significant ($p < 0.05$) separations between control and Fe@Si-NPs-exposed groups in the metabolomes of biological tissues including spleen, liver, kidney, and lung. The corresponding volcano plots indicate the biochemical alterations following the administration of Fe@Si-NPs by the significant class-discriminating metabolites in the different bio-compartments (right panels in Figure 6). And the detailed bio-information of the discriminatory metabolites was displayed in Table S4 in the supplemental materials.

As identified by the biodistribution results, spleen, and liver are the targeted-organs of the Fe@Si-NPs. Therefore, the metabolic variations of endogenous metabolites in the rat spleen and liver could reflect the overall biological effects related to the biodistribution of Fe@Si-NPs. In spleen, a significant elevation in the levels of 3-methylhistidine, cytidine, ethanolamine, GSH, histidine, *myo*-inositol, propionate, threonine, and β -glucose and a significant reduction in the levels of adenosine monophosphate (AMP), deoxyguanosine, glutamate, glycerophosphocholine (GPC), lactate, nicotinamide adenine dinucleotide (NAD), phosphocholine (PC), and phosphoethanolamine (PEA) were observed in the Fe@Si-NPs-treated groups. In liver, the metabolic variations in Fe@Si-NPs groups were highlighted by higher levels of glycine and N-stearoylsphingosine (NSP), and lower levels of GSH, lactate, *myo*-inositol, PC, α -& β -glucose.

GSH plays a pivotal role in maintaining the bio-redox state and is identified as conjugating substances in detoxification (MacIntyre et al. 2011). A dose-dependent change of GSH in liver, spleen, and lung was observed during the exposure of Fe@Si-NPs, which may suggest an accelerated conjugation reaction in detoxification in higher dose of Fe@Si-NPs exposure.

As a phosphagen, PC is biosynthesized by choline kinase converting ATP and choline into PC and ADP. Ethanolamine and PC are components for the synthesis of phospholipids (Norikura et al. 2007).

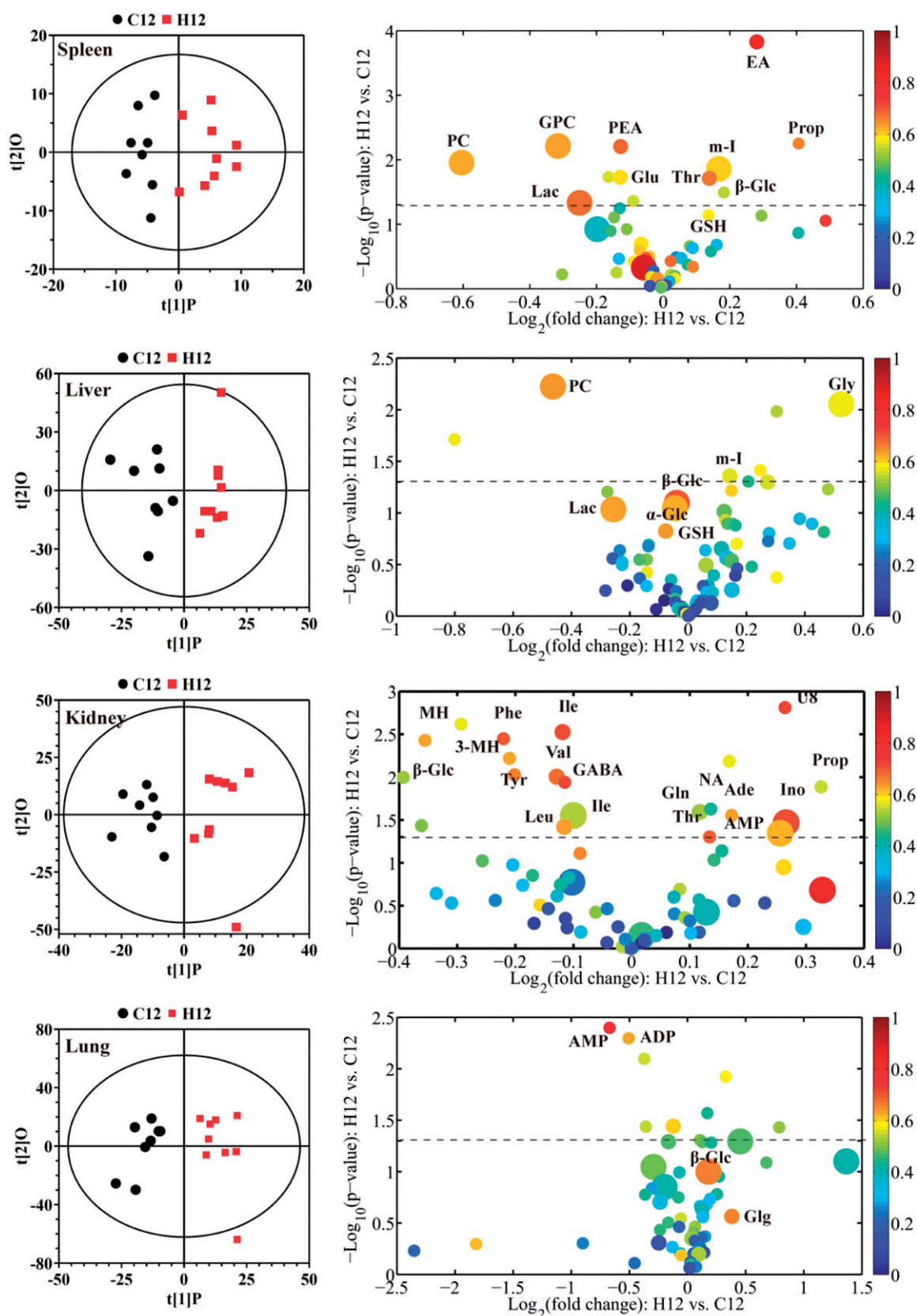


Figure 6. OPLS-DA scores plots (left panels) and corresponding volcano plots (right panels) derived from ^1H NMR spectra of rat tissues at 12th week post-dose obtained from the different pair-wise groups. C, L, and H represent the control, low-, and high-dose groups, respectively. The marked circles in the volcano plots represent the differential metabolites. Keys for the assignments are shown in Table S1 in the supplemental materials.

PEA is an ethanolamine derivative. GPC is a supportive nutrient for organs and a building block for cell membrane phospholipids. A dose-dependent change of PC, ethanolamine and PEA was also observed during the exposure of Fe@Si-NPs (Table S4), which means an enhanced stress-response including cellular membrane modification in the high-dose group.

Usually, the concentration of lactate is governed by oxidative capacity of tissues. Depleted levels of lactate in treated group provided evidence for Fe@Si-NPs restraining anaerobic metabolism. Glucose plays a central function in producing energy. The alteration of lactate and glucose probably signaled the disturbance in energy metabolism. NAD is a coenzyme involved in redox reactions. A dose-dependent change of propanoate and NAD (Table S4) indicates that Fe@Si-NPs impact the nicotinate metabolism of rats. Besides, large doses of *myo*-inositol have been studied for treatment of depression (Gault et al. 2010).

Totally 16 metabolites changed in kidney in a dose-dependent manner in 12 week p. d., including

the decreased concentrations of 1-&3-methylhistidine, glutamate, isoleucine, leucine, phenylalanine, tyrosine, valine and γ -Aminobutyrate (GABA) and the increased concentrations of adenosine, AMP, glutamine, inosine, niacinamide, propionate, threonine, and β -glucose. In comparison, smaller effects were observed in lung metabonomes, in which Fe@Si-NPs induced the increased levels of betaine, glutamate, GSH, GPC, glycogen, *myo*-inositol, propionate, and glucose, and the decreased levels of adenosine diphosphate (ADP), AMP, and taurine.

AMP plays an important role in many cellular metabolic processes and as a monomer in the production of RNA. Inosine is an intermediate in a chain of purine nucleotides reaction. Glutamine is a core link between carbon metabolism of carbohydrates and proteins. The changes of these metabolites related to purine metabolism indicated that Fe@Si-NPs affect protein metabolism of rats. Protein involved in a biochemical reaction with purines, in which the degradation of purines leads to uric acid, which is degraded further to the excretory product allantoin.

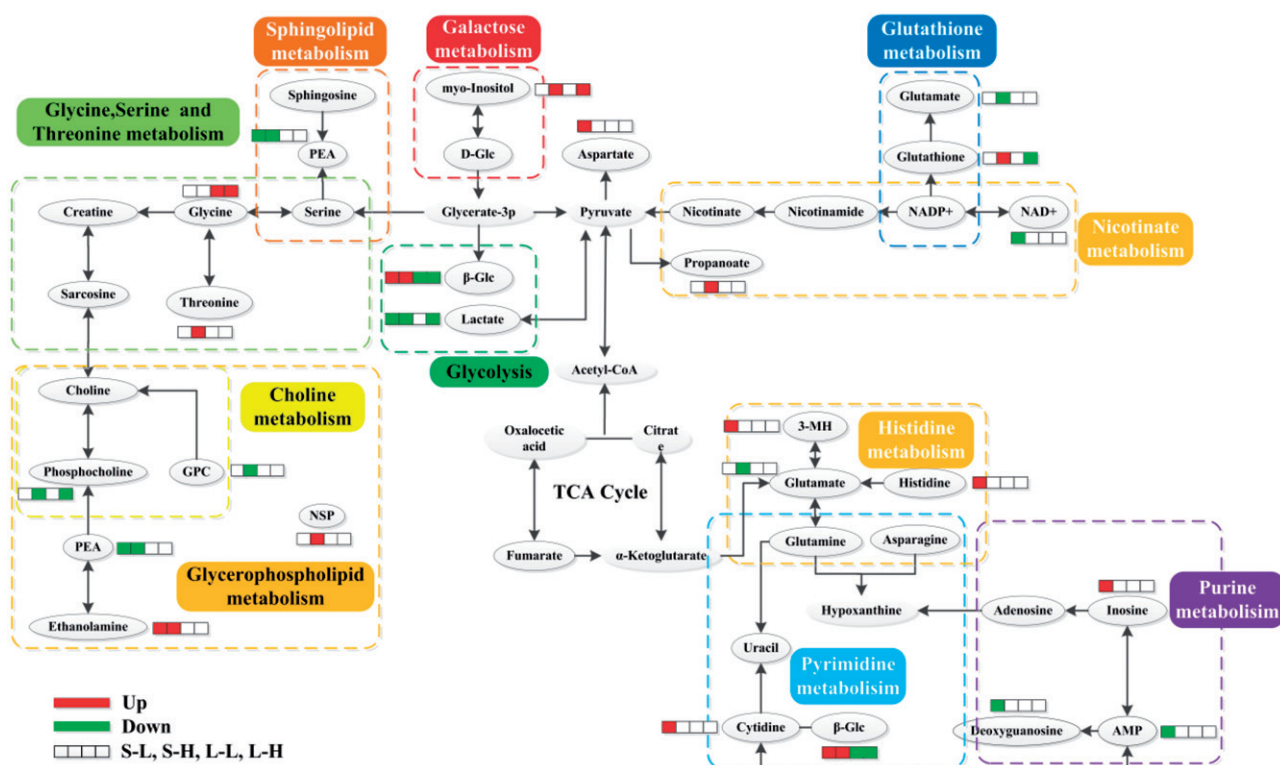


Figure 7. The metabolic networks involved in biodistribution of Fe@Si-NPs via the metabonomic variations in spleen and liver at 12th week post-dose. S- and L- represent the spleen- and liver-tissue, and L and H represent the low- and high-dose groups, respectively. The decreased and increased levels and no significant change of the differential metabolites against the corresponding controls are represented by green, red and blank boxes. The different background colors for the pathways indicate the different biochemical pathways. Keys for the assignments are shown in Table S1 in the supplemental materials.

GABA is a common intermediate of polyamines and plays an essential role in promoting cell growth. It has showed the cytoprotective effect against xenobiotic detoxification by modulating the cellular polyamine levels (Kolter and Sandhoff 2006). Therefore, the increased level of GABA in kidney may be protectively against the bioeffect of Fe@Si-NPs. Glycogen is the polymer of glucose and the primary carbohydrate storage form in animals. It provides an alternative source of glucose other than produced via gluconeogenesis. A decreased level of glycogen in lung was consistent with that Fe@Si-NPs exposure caused an increase in the energy consumption.

3.3.5. The metabolic networks involved in the bio-distribution of Fe@Si-NPs

As the targeted organs of Fe@Si-NPs, the metabolic networks derived from the metabonomic variations of spleen and liver will help to understand their biological fate following depositing in the tissues. As displayed in the metabolic networks (Figure 7), Fe@Si-NPs mainly induced the disturbances in glycerophospholipid and sphingolipid metabolism, metabolisms of purine, pyrimidine, and nicotinate, besides the common energy metabolism such as amino acid metabolisms and glycolysis. Glycerophospholipid and sphingolipid play significant roles in membrane structure and biology and provide many bioactive metabolites (Gault et al. 2010). The disorders in glycerophospholipid and sphingolipid metabolisms probably indicate the troubles in the regulation of membrane proteins and cell function (Kolter and Sandhoff 2006). Purine, pyrimidine, and nicotinate metabolisms are related to degradation of nucleosides and salvage pathways of nucleoside synthesis. And they are usually stringently regulated and coordinated by feedback mechanisms that ensure their appropriate quantities to varying physiological demand (Chapman et al. 1981). Their imbalances may imply that Fe@Si-NPs induced the impairment of the corresponding synthetase thus disturbing the pool sizes of nucleotide triphosphates.

4. Conclusions

The results from biofluids indicated that the 4th week p. d. is a critical time point for transportation,

absorption, and excretion of Fe@Si-NPs. Urine metabonome displayed a metabolic recovery while self-regulation of plasma metabonome led to the parallel metabolic trends between dosed and control groups in 12 weeks p. d. The biological tissue analysis indicated that liver and spleen are the targeted-organs of Fe@Si-NPs. The obvious metabolic variations were induced by Fe@Si-NPs although no visible toxic effects were observed in these tissues over 12 weeks. Furthermore, the metabolic perturbations were involved in glycerophospholipid and sphingolipid metabolism, metabolisms of purine, pyrimidine, and nicotinate besides the common energy metabolism in rats responding to the xenobiotics in organisms. These studies provide preliminary validation for the potential use of Fe@Si-NPs in clinical medicine. And the obtained metabolic information would provide identifiable proof for candidate selection and optimization in the bio-nanoagent development.

Acknowledgments

We thank the help from Drs. Binghui Wu and Nanfeng Zheng of Xiamen University in the synthesis of bio-nanomaterials.

Disclosure statement

No potential conflict of interest was reported by the authors.

Funding

This work was supported by the National Natural Science Foundation of China (Nos. 31671920, 11675135 and U1632274) and the Fundamental Research Funds for the Central Universities (No. 20720150018).

References

- Abramson, S., W. Safrdou, B. Malezieux, V. Dupuis, S. Borensztajn, E. Briot, and A. Bee. 2011. "An Eco-Friendly Route to Magnetic Silica Microspheres and Nanospheres." *Journal of Colloid and Interface Science* 364 (2): 324–332.
- Ahamed, M., M. J. Akhtar, M. A. Siddiqui, J. Ahmad, J. Musarrat, A. A. Al-Khedhairi, M. S. Alsali, and S. A. Alrokayan. 2011. "Oxidative Stress Mediated Apoptosis Induced by Nickel Ferrite Nanoparticles in Cultured A549 Cells." *Toxicology* 283 (2–3): 101–108.
- Chapman, A. G., E. Westerberg, and B. K. Siesjö. 1981. "The Metabolism of Purine and Pyrimidine Nucleotides in Rat Cortex during Insulin-Induced Hypoglycemia and Recovery." *Journal of Neurochemistry* 36 (1): 179–189.

- Chen, J., X. Dong, J. Zhao, and G. Tang. 2009. "In Vivo Acute Toxicity of Titanium Dioxide Nanoparticles to Mice after Intraperitoneal Injection." *Journal of Applied Toxicology* 29 (4): 330–337.
- Chen, Z., H. A. Meng, G. M. Xing, C. Y. Chen, Y. L. Zhao, G. A. Jia, T. C. Wang, et al. 2006. "Acute Toxicological Effects of Copper Nanoparticles in Vivo." *Toxicology Letters* 163 (2): 109–120.
- Craig, SaS. 2004. "Betaine in Human Nutrition." *The American Journal of Clinical Nutrition* 80 (3): 539–549.
- Eckerle, A. 2001. "Ullmann's Encyclopedia of Industrial Chemistry: From Print to Electronic." *Abstracts of Papers of the American Chemical Society* 221: U282–U282.
- Feng, J. H., X. J. Li, F. K. Pei, X. Chen, S. L. Li, and Y. X. Nie. 2002. "H-1 NMR Analysis for Metabolites in Serum and Urine from Rats Administrated Chronically with $\text{La}(\text{NO}_3)_3$." *Analytical Biochemistry* 301 (1): 1–7.
- Gault, C. R., L. M. Obeid, and Y. A. Hannun. 2010. An Overview of Sphingolipid Metabolism: From Synthesis to Breakdown. *Oxygen Transport to Tissue XXXIII* 688:1–23.
- Grabowska, A., M. Nowicki, and J. Kwinta. 2011. "Glutamate Dehydrogenase of the Germinating Triticale Seeds: gene Expression, Activity Distribution and Kinetic Characteristics." *Acta Physiologiae Plantarum* 33 (5): 1981–1990.
- Gupta, A. K., and M. Gupta. 2005. "Synthesis and Surface Engineering of Iron Oxide Nanoparticles for Biomedical Applications." *Biomaterials* 26 (18): 3995–4021.
- Gurung, R. B., B. Purbe, P. Gyawali, and P. Risal. 2013. "The Ratio of Aspartate Aminotransferase to Alanine Aminotransferase (AST/ALT): the Correlation of Value with Underlying Severity of Alcoholic Liver Disease." *Kathmandu University Medical Journal* 11 (3): 233.
- Hirn, S., M. Semmler-Behnke, C. Schleh, A. Wenk, J. Lipka, M. Schaeffler, S. Takenaka, et al. 2011. "Particle Size-Dependent and Surface Charge-Dependent Biodistribution of Gold Nanoparticles after Intravenous Administration." *European Journal of Pharmaceutics and Biopharmaceutics* 77 (3): 407–416.
- Hu, C., J. Deng, Y. Zhao, L. Xia, K. Huang, S. Ju, and N. Xiao. 2014. "A Novel Core-Shell Magnetic Nano-Sorbent with Surface Molecularly Imprinted Polymer Coating for the Selective Solid Phase Extraction of Dimetridazole." *Food Chemistry* 158: 366–373.
- Javidi, J., M. Esmaeilpour, and M. R. Khansari. 2015. "Synthesis, Characterization and Application of Core-Shell Magnetic Molecularly Imprinted Polymers for Selective Recognition of Clozapine from Human Serum." *Rsc Advances* 5 (89): 73268–73278.
- Kand'ar, R., and P. Zakova. 2008. "Allantoin as a Marker of Oxidative Stress in Human Erythrocytes." *Clinical Chemistry and Laboratory Medicine* 46: 1270–1274.
- Khlebtsov, N., and L. Dykman. 2011. "Biodistribution and Toxicity of Engineered Gold Nanoparticles: A Review of in Vitro and in Vivo Studies." *Chemical Society Reviews* 40 (3): 1647–1671.
- Kim, J., H. S. Kim, N. Lee, T. Kim, H. Kim, T. Yu, I. C. Song, W. K. Moon, and T. Hyeon. 2008. "Multifunctional Uniform Nanoparticles Composed of a Magnetite Nanocrystal Core and a Mesoporous Silica Shell for Magnetic Resonance and Fluorescence Imaging and for Drug Delivery." *Angewandte Chemie International Edition* 47 (44): 8322–8441.
- Kolter, T., and K. Sandhoff. 2006. "Sphingolipid Metabolism Diseases." *Biochimica et Biophysica Acta* 1758 (12): 2057–2079.
- Kong, X., R. Gao, X. He, L. Chen, and Y. Zhang. 2012. "Synthesis and Characterization of the Core-Shell Magnetic Molecularly Imprinted Polymers (Fe_3O_4 @MIPs) Adsorbents for Effective Extraction and Determination of Sulfonamides in the Poultry Feed." *Journal of Chromatography A* 1245: 8–16.
- Koplove, H. M. 1984. "Principle of Biochemistry – Lehninger, AL." *Chemical Engineering* 91: 145–146.
- Liu, J., B. Wang, S. B. Hartono, T. Liu, P. Kantharidis, A. P. J. Middelberg, G. Q. Lu, L. He, and S. Z. Qiao. 2012. "Magnetic Silica Spheres with Large Nanopores for Nucleic Acid Adsorption and Cellular Uptake." *Biomaterials* 33 (3): 970–978.
- Li, J., Z. Zhao, J. Feng, J. Gao, and Z. Chen. 2013. "Understanding the Metabolic Fate and Assessing the Biosafety of MnO Nanoparticles by Metabonomic Analysis." *Nanotechnology* 24 (45): 455102.
- Li, J., Z. Zhou, J. Feng, S. Cai, J. Gao, and Z. Chen. 2014. "NMR-Based Metabonomic Analysis of MnO-Embedded Iron Oxide Nanoparticles as Potential Dual-Modal Contrast Agents." *Journal of Nanoparticle Research* 16 (5): 2411.
- Macintyre, L., L. A. Zheng, P. Scullion, P. Keating, and D. G. Watson. 2011. "Metabolomic Profiling of Biomarkers of Liver X Receptor-Induced Toxicity in Mouse Liver Tissue." *Metabolomics* 7 (1): 54–70.
- Moyano, D. F., M. Goldsmith, D. J. Solfiell, D. Landesman-Milo, O. R. Miranda, D. Peer, and V. M. Rotello. 2012. "Nanoparticle Hydrophobicity Dictates Immune Response." *Journal of the American Chemical Society* 134 (9): 3965–3967.
- Norikura, T., A. Kojima-Yuasa, D. O. Kennedy, and I. Matsui-Yuasa. 2007. "Protective Effect of Gamma-Aminobutyric Acid (GABA) against Cytotoxicity of Ethanol in Isolated Rat Hepatocytes Involves Modulations in Cellular Polyamine Levels." *Amino Acids* 32 (3): 419–423.
- Oberdorster, G., A. Maynard, K. Donaldson, V. Castranova, J. Fitzpatrick, K. Ausman, J. Carter, Toxicity, I.R.F.R.S.I.N. & Screening Working Group, et al. 2005. "Principles for Characterizing the Potential Human Health Effects from Exposure to Nanomaterials: Elements of a Screening Strategy." *Particle and Fibre Toxicology* 2 (1): 8–8.
- Saini, S., R. Sharma, R. L. Baron, D. A. Turner, P. R. Ros, P. F. Hahn, W. C. Small, et al. 2000. "Multicentre Dose-Ranging Study on the Efficacy of USPIO Ferumoxtran-10 for Liver MR Imaging." *Clinical Radiology* 55 (9): 690.
- Schindhelm, R. K., M. Diamant, J. M. Dekker, M. E. Tushuizen, T. Teerlink, and R. J. Heine. 2006. "Alanine Aminotransferase

- as a Marker of Non-Alcoholic Fatty Liver Disease in Relation to Type 2 Diabetes Mellitus and Cardiovascular Disease." *Diabetes/Metabolism Research and Reviews* 22 (6): 437–443.
- Shao, M., J. Han, M. Wei, D. G. Evans, and X. Duan. 2011. "The Synthesis of Hierarchical Zn-Ti Layered Double Hydroxide for Efficient Visible-Light Photocatalysis." *Chemical Engineering Journal* 168 (2): 519–524.
- Shi, H., R. Magaye, V. Castranova, and J. Zhao. 2013. "Titanium Dioxide Nanoparticles: A Review of Current Toxicological Data." *Particle and Fibre Toxicology* 10 (1): 15.
- Slováková, M., M. Sedlák, B. Krížková, R. Kupčík, R. Bulánek, L. Korecká, Č. Drašar, and Z. Bílková. 2015. "Application of Trypsin $\text{Fe}_3\text{O}_4@\text{SiO}_2$ Core/Shell Nanoparticles for Protein Digestion." *Process Biochemistry* 50 (12): 2088–2098.
- Sonavane, G., K. Tomoda, and K. Makino. 2008. "Biodistribution of Colloidal Gold Nanoparticles after Intravenous Administration: Effect of Particle Size." *Colloids and Surfaces B-Biointerfaces* 66 (2): 274–280.
- Sreekumar, A., L. M. Poisson, T. M. Rajendiran, A. P. Khan, Q. Cao, J. D. Yu, B. Laxman, et al. 2009. "Metabolomic Profiles Delineate Potential Role for Sarcosine in Prostate Cancer Progression." *Nature* 457 (7231): 910–914.
- Van Der Zande, M., R. J. Vandebriel, E. Van Doren, E. Kramer, Z. H. Rivera, C. S. Serrano-Rojero, E. R. Gremmer, et al. 2012. "Distribution, Elimination, and Toxicity of Silver Nanoparticles and Silver Ions in Rats after 28-Day Oral Exposure." *Acs Nano* 6 (8): 7427–7442.
- Vivero-Escoto, J. L., and Y. T. Huang. 2011. "Inorganic-Organic Hybrid Nanomaterials for Therapeutic and Diagnostic Imaging Applications." *International Journal of Molecular Sciences* 12 (6): 3888–3927.
- Wang, F., X. L. Chen, Z. X. Zhao, S. H. Tang, X. Q. Huang, C. H. Lin, C. B. Cai, and N. F. Zheng. 2011. "Synthesis of Magnetic, Fluorescent and Mesoporous Core-Shell-Structured Nanoparticles for Imaging, Targeting and Photodynamic Therapy." *Journal of Materials Chemistry* 21 (30): 11244–11252.
- Wang, L.-L., Q.-L. Yu, L. Han, X.-L. Ma, R.-D. Song, S.-N. Zhao, and W.-H. Zhang. 2018. "Study on the Effect of Reactive Oxygen Species-Mediated Oxidative Stress on the Activation of Mitochondrial Apoptosis and the Tenderness of Yak Meat." *Food Chemistry* 244: 394–402.
- Wang, Y., M. Zhang, L. Wang, W. Li, J. Zheng, and J. Xu. 2015. "Synthesis of Hierarchical Nickel Anchored on $\text{Fe}_3\text{O}_4@\text{SiO}_2$ and Its Successful Utilization to Remove the Abundant Proteins (BHb) in Bovine Blood." *New Journal of Chemistry* 39 (6): 4876–4881.
- Williams, A. L., and J. H. Hoofnagle. 1988. "Ratio of Serum Aspartate to Alanine Aminotransferase in Chronic Hepatitis. Relationship to Cirrhosis." *Gastroenterology* 95 (3): 734–739.
- Wu, H., L. Tang, L. An, X. Wang, H. Zhang, J. Shi, and S. Yang. 2012. "pH-Responsive Magnetic Mesoporous Silica Nanospheres for Magnetic Resonance Imaging and Drug Delivery." *Reactive & Functional Polymers* 72 (5): 329–336.
- Xie, G. P., J. Sun, G. R. Zhong, L. Y. Shi, and D. W. Zhang. 2010. "Biodistribution and Toxicity of Intravenously Administered Silica Nanoparticles in Mice." *Archives of Toxicology* 84 (3): 183–190.
- Xiong, L. Q., T. S. Yang, Y. Yang, C. J. Xu, and F. Y. Li. 2010. "Long-Term in Vivo Biodistribution Imaging and Toxicity of Polyacrylic Acid-Coated Upconversion Nanophosphors." *Biomaterials* 31 (27): 7078–7085.
- Xu, H., W. J. Yan, P. H. Zhang, and W. R. Huang. 2012. "Adsorption Property of Amino-Modified $\text{Fe}_3\text{O}_4@\text{SiO}_2$ Core-Shell Structure about DNA." *Journal of Central South University* 43: 100–104.
- Yang, S. T., X. Wang, G. Jia, Y. Q. Gu, T. C. Wang, H. Y. Nie, C. C. Ge, H. F. Wang, and Y. F. Liu. 2008. "Long-Term Accumulation and Low Toxicity of Single-Walled Carbon Nanotubes in Intravenously Exposed Mice." *Toxicology Letters* 181 (3): 182–189.
- Zhan, S., Y. Yang, Z. Shen, J. Shan, Y. Li, S. Yang, and D. Zhu. 2014. "Efficient Removal of Pathogenic Bacteria and Viruses by Multifunctional Amine-Modified Magnetic Nanoparticles." *Journal of Hazardous Materials* 274: 115–123.
- Zhang, H. W., Y. Liu, and S. H. Sun. 2010. "Synthesis and Assembly of Magnetic Nanoparticles for Information and Energy Storage Applications." *Frontiers of Physics in China* 5 (4): 347–356.
- Žitňanová, I., P. Korytár, O. I. Aruoma, M. Šustrová, I. Garaiová, J. Muchová, T. Kalnovičová, S. Pueschel, and Z. Ďuračková. 2004. "Uric Acid and Allantoin Levels in Down Syndrome: Antioxidant and Oxidative Stress Mechanisms?" *Clinica Chimica Acta* 341 (1-2): 139–146.